Numerical study of droplet impact on a flexible substrate

Yongfeng Xiong, Haibo Huang,* and Xi-Yun Lu
Department of Modern Mechanics, and University of Science and Technology of China, Anhui 230026, China

(Received 27 January 2020; accepted 8 May 2020; published 21 May 2020)

Droplets interacting with deformable moving boundaries is ubiquitous. The flexible boundaries may dramatically affect the hydrodynamic behavior of droplets. A numerical method for simulating droplet impact on flexible substrates is developed. The effect of flexibility is investigated. To reduce the contact time and increase the remaining upward momentum in the flexible cases, the Weber number should be larger than a critical value. Moreover, the ratio of the natural frequency of the plate to that of the droplet F_r should approximately equal to the reciprocal of the contact time of droplets impact on the rigid surfaces (t_{ctr}) at the same We, e.g., $F_r \approx 1/t_{ctr}$. Only under this circumstance would the kinetic energy convert into the surface energy of the droplet and the elastic energy of the plate simultaneously, and vice versa. Moreover, based on a double spring model, we proposed scaling laws for the maximal deflection of the plate and spreading diameter of the drop. Finally, the droplet impact under different wettability is qualitatively studied. We found that the flexibility may contribute to the droplet bouncing at a smaller contact angle.

DOI: 10.1103/PhysRevE.101.053107

I. INTRODUCTION

Droplet impacts on flexible surfaces are very common in industrial and natural systems, such as rain-induced foliar disease transmission [1], anti-icing [2], and ink-jet printing [3]. Droplet impact plays an essential role in the process of mass, momentum, and energy transmission. As a droplet impacts on a rigid surface, its kinetic energy would be converted to surface energy. Its momentum would be redirected to the lateral direction, flattening the shape and spreading to its maximal spreading diameter. Then, it would retract because the surface energy may convert into kinetic energy. The droplet may adhere, bounce off, or splash, which depends on parameters of wettability, viscosity, impact velocity, and surface tension [4,5]. Previous studies have focused mainly on drop-surface contact time, maximal spreading diameter, and splashing.

Some experimental studies focused on the contact time during drop-surface interaction. Richard *et al.* [6] studied the contact time of a droplet impacting on a superhydrophobic surface. They found that the contact time is proportional to inertial-capillary timescale $(\rho_H D_0^3/\sigma)^{1/2}$, where ρ_H, D_0, and σ are density, initial diameter, and surface tension, respectively, of the droplet. The range of the Weber number We is $0.3 \leqslant \mathrm{We} \leqslant 37$ in their experiments. By using superhydrophobic surfaces with a morphology, Bird *et al.* [7] found that it is possible to reduce the contact time by a factor of 1.6 compared to the time of impacting on the flat surface. Similar studies on drop impact on superhydrophobic macrotextures also have been conducted [8,9]. Moreover, Liu *et al.* [10] found that pancake bouncing achieves a fourfold reduction in contact time. By designing surfaces with tapered micro-/nanotextures, the capillary energy could be stored in the penetrated liquid. The stored energy would contribute to the upward motion of the droplet.

Some studies focused on the maximal spreading diameter D_{max} of the droplet. Two typical regimes for spreading were found. One is the viscous regime, in which viscosity and inertia are balanced. Under this circumstance, the normalized maximum spreading diameter D_{max}/D_0 is proportional to $Re^{1/5}$ [11], i.e., $D_{max}/D_0 \sim Re^{1/5}$. The other is the capillary regime, in which the capillary force and inertia are balanced. According to the viewpoint of energy conservation, in this regime $D_{max}/D_0 \sim \mathrm{We}^{1/2}$ [11], while from the viewpoint of momentum conservation, $D_{max}/D_0 \sim \mathrm{We}^{1/4}$ [12]. It is noticed that the viscous and capillary regimes are both extreme situations, and there is a regime in which the viscosity, capillary force, and inertia are all comparable. By interpolating the viscous and capillary regimes, researchers [13,14] have found a universal scaling for drop impact on flat surfaces.

However, in the studies above, all the surfaces were rigid and fixed. In natural and industrial systems, most of the surfaces are flexible, and the effect of flexibility on drop impact dynamics has never been thoroughly investigated. As far as we know, only a few experimental studies for flexible surfaces have been conducted [15–21]. In the presence of flexible surfaces, in addition to the conversion between the kinetic energy and surface energy, there is a conversion between the kinetic energy and substrate deformation energy. According to the experimental study of Vasileiou *et al.* [18], a rational tuning of flexibility can enhance liquid repellency performance, characterized by the reduced contact time, and the increased coefficient of restitution. They proposed the concept of apparent Weber number, which can be used to predict the maximal spreading diameter. They considered the effect of the mass ratio of the plate to the droplet. However, the effect of flexibility has never been investigated systematically. In the experimental study of Weisensee *et al.* [19], the contact time was reduced by a factor of 2 when a droplet is impacting an elastic superhydrophobic surface. The possible reason is that the substrate imparts vertical momentum back to the

*Corresponding author: huanghb@ustc.edu.cn

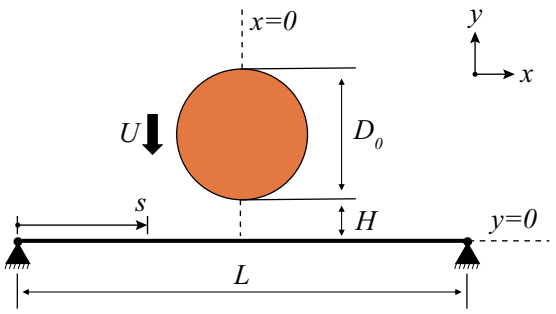

FIG. 1. Schematic diagram for a droplet impacting on the flexible plate. The droplet with diameter D_0 is placed above the flexible plate at a distance $H = 0.2D_0$. The initial downward velocity is U.

droplet with a springboard effect. The phenomenon appears only when We $\geqslant 40$, and $u_s/(gD_{\max})^{1/2} \geqslant 1$, where u_s is the maximum substrate velocity during oscillation and g is the gravitational acceleration. $u_s/(gD_{\max})^{1/2} \geqslant 1$ means the balance between substrate inertia and gravitational force is deduced. Similarly, Huang *et al.* [20] also investigated droplet impact on soft elastic superhydrophobic cotton.

In the studies above, few numerical simulations were performed about a drop impact on flexible surfaces. Compared to the experimental studies, numerical simulations can provide more quantitative information. As far as we know, only one relevant numerical study was carried out by Rosis [22]. However, the density ratio and the viscosity ratio between the two fluids is small. Furthermore, the influence of the contact angle is not considered. Hence, a further numerical investigation of droplets impacting on flexible surfaces is necessary. In the present study, we developed a numerical method that can handle the fluid structure interaction with wetting boundary condition. The purpose of this study is to explore the effects of flexibility, wettability on droplet impact dynamics numerically.

The paper is organized as follows. The physical problem and mathematical formulation are presented in Sec. II. The numerical method and validation are described in Sec. III. Detailed results are discussed in Sec. IV, and concluding remarks are presented in Sec. V.

II. PHYSICAL PROBLEM AND MATHEMATICAL FORMULATION

In our study, the droplet is initially placed above the flexible plate with an initial velocity U (see Fig. 1). To simulate the two-phase flow, we used the following conservative phase-field equation to track the interface between different fluids [23–26]:

$$\frac{\partial \phi}{\partial t} + \nabla \cdot (\phi \boldsymbol{u}) = \nabla \cdot \left[M \left(\nabla \phi - \frac{4}{W} \phi (1-\phi) \hat{\boldsymbol{n}} \right) \right], \quad (1)$$

where ϕ is the component variable varying from 0 to 1, corresponding to light fluid ρ_L and heavy fluid ρ_H, respectively, t time, $\boldsymbol{u}$ macroscopic velocity vector, M mobility, and W interfacial thickness. $\hat{\boldsymbol{n}}$ is the unit vector normal to the interface, with its direction pointing into the heavy fluid, i.e., $\hat{\boldsymbol{n}} = \nabla\phi/|\nabla\phi|$. In diffuse-interface models, the equilibrium phase-field profile is used to initialize the phase field:

$$\phi(\boldsymbol{x}) = \frac{1}{2}\left[1 + \tanh\left(\frac{|\boldsymbol{x} - \boldsymbol{x}_0|}{W/2} \right) \right]. \quad (2)$$

To set a specified contact angle at a boundary, the following contact angle model is used:

$$\hat{\boldsymbol{n}}_w \cdot \nabla\phi|_w = \Theta \phi_w (1 - \phi_w), \quad (3)$$

where $\hat{\boldsymbol{n}}_w$ is the unit vector normal to the solid wall, ϕ_w is the phase-field value at the wall, and Θ is related to the equilibrium contact angle θ_{eq} by

$$\Theta = -\sqrt{\frac{2\beta}{\kappa}} \cos\theta_{\text{eq}}, \quad (4)$$

where β and κ are related to the surface tension σ and the interfacial thickness W by $\beta = 12\sigma/W$ and $\kappa = 3\sigma W/2$.

The isothermal, incompressible Navier-Stokes equations are used to simulate the multiphase flow,

$$\frac{\partial \rho}{\partial t} + \nabla \cdot (\rho \boldsymbol{u}) = 0, \quad (5)$$

$$\rho \left[\frac{\partial \boldsymbol{u}}{\partial t} + \boldsymbol{u} \cdot \nabla(\boldsymbol{u}) \right] = -\nabla p + \nabla \cdot \{\mu[\nabla \boldsymbol{u} + (\nabla \boldsymbol{u})^T]\} + \boldsymbol{f}_s, \quad (6)$$

where ρ is the local fluid density, μ the dynamic viscosity, p the macroscopic pressure, and $\boldsymbol{f}_s$ the surface tension force. The surface tension takes the form of $\boldsymbol{f}_s = \mu_\phi \nabla\phi$ [27,28], where $\mu_\phi = 4\beta\phi(\phi-1)(\phi-1/2) - \kappa\nabla^2\phi$ is the chemical potential for binary fluids. It is noticed that in our simulations there is no gravity.

The structural equation is employed to describe the deformation and motion of the plate [29–31],

$$\rho_s h \frac{\partial^2 \boldsymbol{X}}{\partial t^2} - \frac{\partial}{\partial s}\left[Eh \left(1 - \left| \frac{\partial \boldsymbol{X}}{\partial s} \right|^{-1} \right) \frac{\partial \boldsymbol{X}}{\partial s} \right] + EI \frac{\partial^4 \boldsymbol{X}}{\partial s^4} = \boldsymbol{F}_{\text{ext}}, \quad (7)$$

where s is the Lagrangian coordinate along the plate, $\boldsymbol{X}(s,t) = [X(s,t), Y(s,t)]$ the position vector of the plates, $\boldsymbol{F}_{\text{ext}}$ the external force exerted on the plates by the surrounding fluid, ρ_s the structural density, $\rho_s h$ the structural linear mass density. Eh and EI denote the structural stretching rigidity and bending rigidity, respectively. At both edges of the plate, the simply-supported boundary condition is adopted, i.e.,

$$\boldsymbol{X} = \boldsymbol{X}_0, \frac{\partial^2 \boldsymbol{X}}{\partial s^2} = 0. \quad (8)$$

Furthermore, $\boldsymbol{X}(s,0) = (s - 0.5L, 0)$, $\partial\boldsymbol{X}/\partial t(s,0) = (0,0)$ is the initial condition of the plate. For simply-supported plate on both sides, we can get its natural frequency according to Euler-Bernoulli beam theory, i.e.,

$$w_s = 2\pi f_s = (\beta_n L)^2 \left(\frac{EI}{\rho_s h L^4} \right)^{1/2}, \quad (9)$$

where $\beta_n L = n\pi$. Here, we focus on the first-order natural frequency, corresponding to $n = 1$. The frequency ratio is

$$F_r = \frac{f_s}{f_{\text{ref}}} = \frac{\pi D_0}{2L} \sqrt{\frac{K_B}{M}}, \quad (10)$$

where $f_{\text{ref}} = 1/T_{\text{ref}}$, K_B the bending stiffness, and M the mass ratio.

The characteristic quantities ρ_H, D_0, and U_{ref} are chosen to normalize the above equations. Here ρ_H is the density of the droplet and $U_{\text{ref}} = \sqrt{\sigma/(\rho_H D_0)}$. The characteristic time is $T_{\text{ref}} = D_0/U_{\text{ref}} = \sqrt{\rho_H D_0^3/\sigma}$, which is proportional to the period of droplet vibration. The dimensionless governing parameters are listed as follows: the density ratio between binary fluids $\rho_r = \rho_H/\rho_L$, the dynamic viscosity ratio between binary fluids $\mu_r = \mu_H/\mu_L$, the Weber number $\text{We} = \rho_H U^2 D_0/\sigma = U^2/U_{\text{ref}}^2$, the Reynolds number $Re = \rho_H U D_0/\mu_H$, the initial length of the flexible plate $L_r = L/D_0$, the bending stiffness $K_B = EI/\rho_H U_{\text{ref}}^2 L^3$, the stretching stiffness $K_S = Eh/\rho_H U_{\text{ref}}^2 L$, the mass ratio of the plate to the droplet $M = \rho_s h/\rho_H L$, and the initial height of the drop above the surface $H_r = H/D_0$. It should be noted that we set $t = 0$ at the moment of the droplet impacting on the flexible plate.

III. NUMERICAL METHOD AND VALIDATION

A. Numerical method

In our simulations, the Navier-Stokes equations are solved by the lattice Boltzmann method and the Euler-Bernoulli equation is solved by a finite element method. The conservative phase-field lattice Boltzmann method (LBM) developed by Geiger *et al.* [32] and Fakhari *et al.* [23] was adopted to solve the interface tracking Eq. (1):

$$h_\alpha(\boldsymbol{x} + \boldsymbol{e}_\alpha \delta t, t + \delta t) = h_\alpha(\boldsymbol{x}, t) - \frac{h_\alpha(\boldsymbol{x}, t) - h_\alpha^{\text{eq}}(\boldsymbol{x}, t)}{\tau_\phi + 1/2}, \quad (11)$$

where h_α is the phase-field distribution function, τ_ϕ is the phase-field relaxation time, and $\boldsymbol{e}_\alpha$ is the discrete velocity set. Here the D2Q9 model [23] is adopted. The equilibrium phase-field distribution function [32] is defined as

$$h_\alpha^{\text{eq}} = \phi\Gamma_\alpha + w_\alpha \frac{M}{c_s^2}\left[\frac{4}{W}\phi(1-\phi)\right](\boldsymbol{e}_\alpha \cdot \hat{\boldsymbol{n}}), \quad (12)$$

where

$$\Gamma_\alpha = w_\alpha\left[1 + \frac{\boldsymbol{e}_\alpha \cdot \boldsymbol{u}}{c_s^2} + \frac{(\boldsymbol{e}_\alpha \cdot \boldsymbol{u})^2}{2c_s^4} - \frac{\boldsymbol{u}\cdot\boldsymbol{u}}{2c_s^2}\right], \quad (13)$$

and w_α is the weight coefficient set, where $w_0 = 4/9$, $w_{1-4} = 1/9$, and $w_{5-8} = 1/36$. The mobility $M = \tau_\phi c_s^2 \delta t$, and the speed of sound $c_s = 1/\sqrt{3}$. The component variable ϕ is recovered by

$$\phi = \sum_\alpha h_\alpha, \quad (14)$$

and the density can be calculated by $\rho = \rho_L + \phi(\rho_H - \rho_L)$.

The hydrodynamic dynamic Eqs. (5) and (6) are numerically solved by

$$\bar{g}_\alpha(\boldsymbol{x} + \boldsymbol{e}_\alpha \delta t, t + \delta t) = \bar{g}_\alpha(\boldsymbol{x}, t) + \Omega_\alpha(\boldsymbol{x}, t) + F_\alpha(\boldsymbol{x}, t), \quad (15)$$

where $\bar{g}_\alpha$ is the hydrodynamic distribution function, Ω_α is the multiple-relaxation-time collision operator, taking the form of

$$\Omega_\alpha = -\Lambda_{\beta\alpha}\left(\bar{g}_\alpha - \bar{g}_\alpha^{\text{eq}}\right), \quad (16)$$

where $\Lambda_{\beta\alpha}$ is the collision matrix, and

$$F_\alpha = \delta t\left[(\Gamma_\alpha - w_\alpha)(\rho_H - \rho_L)c_s^2 + \Gamma_\alpha \mu_\phi\right](\boldsymbol{e}_\alpha - \boldsymbol{u}) \cdot \nabla\phi \quad (17)$$

is the forcing term. The modified equilibrium distribution function is defined by $\bar{g}_\alpha^{\text{eq}} = g_\alpha^{\text{eq}} - F_\alpha/2$ and $g_\alpha^{\text{eq}} = pw_\alpha + \rho c_s^2(\Gamma_\alpha - w_\alpha)$. The macrovariables are calculated through

$$\boldsymbol{u} = \frac{1}{\rho c_s^2}\sum_\alpha \bar{g}_\alpha \boldsymbol{e}_\alpha + \frac{\delta t}{2\rho}\boldsymbol{f}_s, \quad (18)$$

$$p = \sum_\alpha \bar{g}_\alpha + \frac{\delta t}{2}(\rho_H - \rho_L)c_s^2 \boldsymbol{u} \cdot \nabla\phi. \quad (19)$$

For more detailed information, please refer to Fakhari's study [23].

The structural Eq. (7) for the flexible substrate is solved by a geometric nonlinear finite element method. Based on the principle of virtual work and shape function approximation, a semidiscrete form of the structural equation at time $t + \Delta t$ can be obtained [33], i.e.,

$$\boldsymbol{M}_1 \ddot{\boldsymbol{a}}_{t+\Delta t} + \boldsymbol{C}\dot{\boldsymbol{a}}_{t+\Delta t} + \boldsymbol{F}_{\text{int},t+\Delta t} - \boldsymbol{F}_{\text{ext},t+\Delta t} = \boldsymbol{0}, \quad (20)$$

where $\boldsymbol{a}$ is the displacement vector, $\boldsymbol{M}_1$ is the mass matrix, $\boldsymbol{C}$ is the damping matrix, $\boldsymbol{F}_{\text{int}}$ is the internal force, and $\boldsymbol{F}_{\text{ext}}$ is the external force exerted on the beam. The nonlinear term $\boldsymbol{F}_{\text{int}}$ is solved through the Newton-Raphson method [33]. A second-order unconditionally stable direct numerical integration method, i.e., the Newmark-β method, is adopted. The final iterative solution equation is as follows:

$$\begin{aligned}&\left[c_0\boldsymbol{M}_1 + c_1\boldsymbol{C} + \boldsymbol{K}_{T,t+\Delta t}^{(i)}\right]\Delta\boldsymbol{a}^{(i+1)}\\ &= \boldsymbol{F}_{\text{ext},t+\Delta t} + \boldsymbol{F}_{\text{int},t+\Delta t}^{(i)} - \boldsymbol{M}_1\left[c_0\left(\boldsymbol{a}_{t+\Delta t}^{(i)} - \boldsymbol{a}_t\right) - c_2\dot{\boldsymbol{a}}_t - c_3\ddot{\boldsymbol{a}}_t\right]\\ &\quad - \boldsymbol{C}\left[c_1\left(\boldsymbol{a}_{t+\Delta t}^{(i)} - \boldsymbol{a}_t\right) - c_4\dot{\boldsymbol{a}}_t - c_5\ddot{\boldsymbol{a}}_t\right], \end{aligned} \quad (21)$$

where $\boldsymbol{K}_T$ is the tangent matrix which is solved by the corotational scheme [33], c_0–c_5 are the coefficients associated with the Newmark method, and the superscript denotes the subiteration time of the beam solver. The update iteration of the variable is

$$\begin{aligned}&\boldsymbol{a}_{t+\Delta t}^{(i+1)} = \boldsymbol{a}_{t+\Delta t}^{(i)} + \Delta\boldsymbol{a}^{(i+1)}, \quad \boldsymbol{K}_{T,t+\Delta t}^{(i)} = \boldsymbol{K}_T\left(\boldsymbol{a}_{t+\Delta t}^{(i)}\right),\\ &\boldsymbol{F}_{\text{int},t+\Delta t}^{(i)} = \boldsymbol{F}_{\text{int}}\left(\boldsymbol{a}_{t+\Delta t}^{(i)}\right), \quad \boldsymbol{X}_{t+\Delta t}^{(i+1)} = \boldsymbol{X}_0 + \boldsymbol{a}_{t+\Delta t}^{(i+1)}, \end{aligned} \quad (22)$$

where $\boldsymbol{X}_0$ is the initial reference position of the beam. The initial iteration is $\boldsymbol{a}_{t+\Delta t}^{(0)} = \boldsymbol{a}_t$. After the iteration is converged, the displacement at new time $\boldsymbol{a}_{t+\Delta t}$ can be obtained. The speed and acceleration can be obtained by

$$\ddot{\boldsymbol{a}}_{t+\Delta t} = c_0(\boldsymbol{a}_{t+\Delta t} - \boldsymbol{a}_t) - c_2\dot{\boldsymbol{a}}_t - c_3\ddot{\boldsymbol{a}}_t, \quad (23)$$

$$\dot{\boldsymbol{a}}_{t+\Delta t} = c_1(\boldsymbol{a}_{t+\Delta t} - \boldsymbol{a}_t) - c_4\dot{\boldsymbol{a}}_t - c_5\ddot{\boldsymbol{a}}_t. \quad (24)$$

The flexible substrate in the flow is a deformable moving boundary. The schematic diagram for a moving deformable boundary immersed in fluid is shown in Fig. 2. Here, the fluid at the boundary should satisfy the nonslip boundary condition, i.e., $\boldsymbol{u} = \boldsymbol{u}_w$, where $\boldsymbol{u}_w$ is the velocity at $\boldsymbol{x}_w$. In the LBM, the the bounce-back method is adopted to ensure the physical nonslip boundary condition. Specifically, in the LBM the distribution functions $h_{\bar{\alpha}}(\boldsymbol{x}_f, t + \delta t) = h_{\bar{\alpha}}^*(\boldsymbol{x}_s, t)$ and $\bar{g}_{\bar{\alpha}}(\boldsymbol{x}_f, t + \delta t) = \bar{g}_{\bar{\alpha}}^*(\boldsymbol{x}_s, t)$ are unknown (see Fig. 2) because

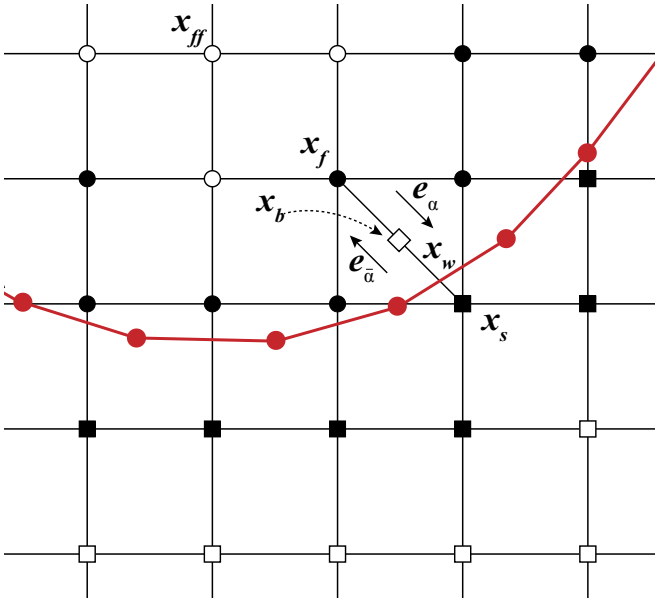

FIG. 2. A moving deformable boundary (solid red line) immersed in fluid. Circles and squares represent fluid and solid points, respectively. Filled black circles and squares are fluid and solid nodes closest to the boundary. $e_{\bar{\alpha}}$ represents the opposite direction of e_α. Filled red circles represent the Lagrangian points on the moving deformable boundary. $\boldsymbol{x}_w$ is the intersection of the link from $\boldsymbol{x}_f$ to $\boldsymbol{x}_s$ and the boundary.

in the LBM, the evolution equation (the lattice Boltzmann equation) is not performed on the solid nodes. So we have to specify these unknowns. Here the unknown phase-field distribution function $h^*_{\bar{\alpha}}(\boldsymbol{x}_s, t)$ is given by

$$h^*_{\bar{\alpha}}(\boldsymbol{x}_s) = h^*_\alpha(\boldsymbol{x}_f) + 2\frac{\phi(\boldsymbol{x}_f)}{c_s^2} w_\alpha(\boldsymbol{u}_b \cdot \boldsymbol{e}_{\bar{\alpha}}), \tag{25}$$

where $\boldsymbol{u}_b$ is the velocity at $\boldsymbol{x}_b$, the middle of the link between $\boldsymbol{x}_f$ and $\boldsymbol{x}_s$ [34]. It is noted that if $\boldsymbol{u}_b = 0$, Eq. (25) becomes midway bounce back for a static wall. In the studies of particles interacting with the fluid, the particle is rigid, so $\boldsymbol{u}_b$ can be calculated by the particle position and velocity. However, here the boundary is deformable and $\boldsymbol{u}_b$ is obtained through interpolation

$$\boldsymbol{u}_b(\boldsymbol{x}_b) = \frac{\sum_X [\boldsymbol{u}(\boldsymbol{X})/(\boldsymbol{X} - \boldsymbol{x}_b)^2]}{\sum_X [1/(\boldsymbol{X} - \boldsymbol{x}_b)^2]}, \tag{26}$$

where $\boldsymbol{X}$ and $\boldsymbol{u}(\boldsymbol{X})$ are the position and velocity of the Lagrangian nodes [35–37], respectively.

The unknown hydrodynamic distribution function $\bar{g}^*_{\bar{\alpha}}(\boldsymbol{x}_s, t)$ can be obtained using the scheme of Mei *et al.* [23,38], i.e.,

$$\bar{g}^*_{\bar{\alpha}}(\boldsymbol{x}_s) = (1-\chi)\bar{g}^*_\alpha(\boldsymbol{x}_f) + \chi\tilde{g}_\alpha(\boldsymbol{x}_{bf}) + 2\frac{\rho(\boldsymbol{x}_f)}{c_s^2} w_\alpha(\boldsymbol{u}_w \cdot \boldsymbol{e}_{\bar{\alpha}}), \tag{27}$$

where χ is the weighting factor, and

$$\tilde{g}_\alpha(\boldsymbol{x}_{bf}) = g^{\mathrm{eq}}_\alpha(\boldsymbol{x}_f) + \rho(\boldsymbol{x}_f) w_\alpha \boldsymbol{e}_\alpha \cdot (\boldsymbol{u}_{bf} - \boldsymbol{u}_f), \tag{28}$$

where $\boldsymbol{u}_{bf}$ is obtained by interpolation. Through the momentum exchange method [34,39–41], the external force exerted on the substrate can be obtained,

$$\boldsymbol{F}(\boldsymbol{e}_\alpha; \boldsymbol{x}_w) = (\boldsymbol{e}_\alpha - \boldsymbol{u}_w)\bar{g}^*_\alpha(\boldsymbol{x}_f) - (\boldsymbol{e}_{\bar{\alpha}} - \boldsymbol{u}_w)\bar{g}^*_{\bar{\alpha}}(\boldsymbol{x}_s). \tag{29}$$

Then, $\boldsymbol{F}(\boldsymbol{e}_\alpha; \boldsymbol{x}_w)$ is linearly distributed to two adjacent Lagrangian nodes. To investigate the effect of wettability, we incorporated the contact angle model into our algorithm [see Eq. (3)]. To enhance the numerical accuracy and stability, we adopted a weighted least square method (LSM) [42–44] to integrate the contact angle model. The details can be found in the Appendix.

It is noticed that in the momentum exchange method, only the hydrodynamic force is considered, but the surface tension force exerted on the substrate is not included. There are two ways to calculate the capillary force. One is the sharp interface method, e.g., $\boldsymbol{F}_{\mathrm{ST}} = \sigma\boldsymbol{m}$, where $\boldsymbol{m}$ is a unit vector tangent to the local interface, and points out from the boundary. The other is the diffuse interface scheme [34]:

$$\boldsymbol{F}_{\mathrm{ST}} = \int_{\phi=0}^{1} w(\phi)\sigma\boldsymbol{m}(\phi)d\phi \approx \sum_i^N w(\phi_i)\sigma\bar{\boldsymbol{m}}(\phi_i)\sin(\theta), \tag{30}$$

where N is the number of cells across the interface, $w(\phi)$ is the weight function which satisfies $\int_{\phi=0}^{1} w(\phi)d\phi = 1$. $\bar{\boldsymbol{m}}(\phi_i) = (-\frac{\partial\phi}{\partial y}, \frac{\partial\phi}{\partial x})$ for $\frac{\partial\phi}{\partial x} > 0$; otherwise, $\bar{\boldsymbol{m}}(\phi_i) = (\frac{\partial\phi}{\partial y}, -\frac{\partial\phi}{\partial x})$. In the study of Connington *et al.* [34], the contact angle is 90°, so N is approximately equal to the interface thickness W. However, for other contact angles, the number of cells across the interface along the moving boundary is $N = W/\sin(\theta)$. Considering the influence of the contact angle, we have Eq. (30).

Because the boundary is moving, some solid nodes in the area swept by the boundary may become fluid nodes. Under this circumstance, the density, velocity, pressure, and distribution functions are unknown at these new fluid nodes which are marked as $\boldsymbol{x}_{s\to f}$. The density is specified as $\rho(\boldsymbol{x}_{s\to f}, t+\delta t) = \bar{\rho}(\boldsymbol{x}_s, t)$, where $\bar{\rho}(\boldsymbol{x}_s, t)$ is obtained by applying the wetting boundary condition Eq. (3) at solid boundary nodes. Because the new nodes are very close to the moving boundary, the velocity on these nodes is approximately equal to that of the wall, e.g., $\boldsymbol{u}(\boldsymbol{x}_{s\to f}, t+\delta t) = \boldsymbol{u}[\boldsymbol{X}(\boldsymbol{x}_s), t+\delta t]$. The pressure is assumed to be $p(\boldsymbol{x}_{s\to f}, t+\delta t) = \sum_i p(\boldsymbol{x}_{f_i}, t+\delta t)/N_{\mathrm{pre}}$, where N_{pre} represents the number of old fluid nodes x_{f_i} around $x_{s\to f}$. Then, the distribution functions of the new nodes are supposed to be the local equilibrium distribution function [34,45,46], which are assumed to be a function of the macrovariables.

To handle such a coupling problem, we use subiterations between fluid (LBM) and beam (FEM) solvers [47]. Suppose at time t, a Lagrange point located at $\boldsymbol{X}(t)$ in the beam has velocity $\boldsymbol{u}(t)$. We take it as an example to illustrate the details. The following sequential steps would be performed.

(1) Step A: The lattice Boltzmann equation is solved and the bounce-back method [Eqs. (25) and (27)] for moving boundaries is adopted to achieve the nonslip boundary condition.

(2) Step B: The external force (load) $\boldsymbol{F}_{\mathrm{ext}}$ exerted on $\boldsymbol{X}$ is obtained by the momentum exchange method [Eq. (29)] at the same time.

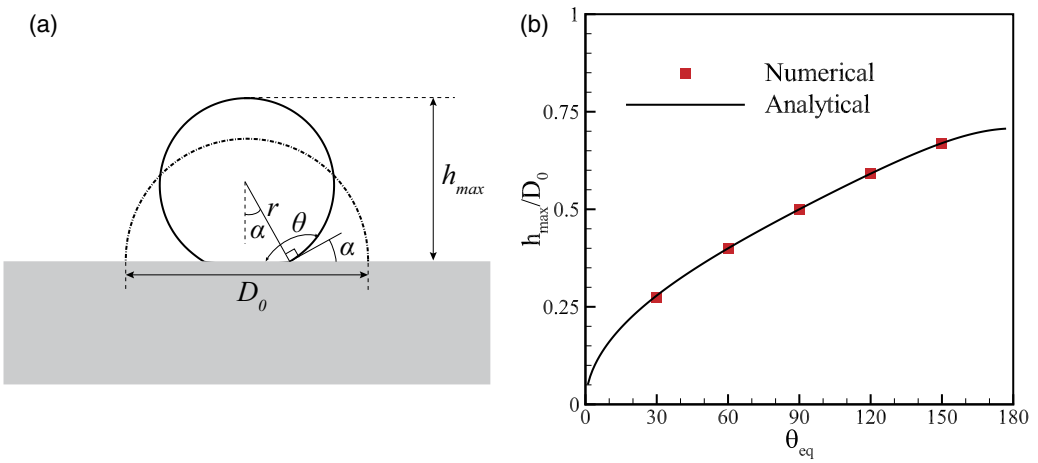

FIG. 3. (a) A droplet with contact angle θ_{eq} rests on a flat surface. The dash-dotted and solid lines ($\phi = 0.5$) represent the drop's initial and equilibrium ($t = 50T_{ref}$) shapes, respectively. (b) The ratio of height to initial diameter as a function of contact angle.

(3) Step C: Using the load $\boldsymbol{F}_{ext}$ and the finite element method, $\boldsymbol{X}$ and $\boldsymbol{u}$ are updated.

To get the correct $\boldsymbol{X}(t+\Delta t)$ and $\boldsymbol{u}(t+\Delta t)$ at time step $t+\Delta t$, we did use the following subiterations. First, after Steps A and B are implemented, using the FEM and $\boldsymbol{F}_{ext}(t)$ (Step C) we have velocity $\boldsymbol{u}^{(1)}(t+\Delta t)$ and $\boldsymbol{X}^{(1)}(t+\Delta t)$, where the superscript denotes the subiteration time. Second, using $\boldsymbol{u}^{(1)}(t+\Delta t)$ and $\boldsymbol{X}^{(1)}(t+\Delta t)$ and implementing Steps A and B, we have $\boldsymbol{F}^{(1)}_{ext}(t+\Delta t)$. Using $\boldsymbol{F}^{(1)}_{ext}(t+\Delta t)$ and Step C we have $\boldsymbol{u}^{(2)}(t+\Delta t)$ and $\boldsymbol{X}^{(2)}(t+\Delta t)$, which may be different from $\boldsymbol{u}^{(1)}(t+\Delta t)$ and $\boldsymbol{X}^{(1)}(t+\Delta t)$, respectively. At the kth subiteration we check whether $|\boldsymbol{u}^{(k)}(t+\Delta t) - \boldsymbol{u}^{(k-1)}(t+\Delta t)| < \epsilon_1$ or $|\boldsymbol{X}^{(k)}(t+\Delta t) - \boldsymbol{X}^{(k-1)}(t+\Delta t)| < \epsilon_2$ reaches, where ϵ_1, ϵ_2 are specified small parameters. When the convergency is reached, we set $\boldsymbol{u}(t+\Delta t) = \boldsymbol{u}^{(k)}(t+\Delta t)$ and $\boldsymbol{X}(t+\Delta t) = \boldsymbol{X}^{(k)}(t+\Delta t)$ and continue the next-time-step simulation.

The above iterations between the beam and fluid solvers do guarantee the flow speed along the interface is almost identical. In this way, the interface condition is satisfied.

The computational domain is chosen as $-3.5D \leqslant x \leqslant 3.5D$ and $-1.0D \leqslant y \leqslant 6.0D$. The domain is large enough to eliminate the boundary effect. The boundary condition $\boldsymbol{u} = 0$ is applied on the left and right boundary. For the top boundary, the outflow boundary conditions $\partial h_\alpha/\partial y = 0$ and $\partial \bar{g}_\alpha/\partial y = 0$ are used. The mesh spacing $\delta x = 1\,lu$ and time step $\delta t = 1\,ts$ are lattice units used in the LBM. The normalized grid spacings in the x and y direction is uniform with $\Delta x = \Delta y = \delta x/L_{ref} = 0.015625$. The normalized time step is $\Delta t = \delta t/T_{ref} = 1.171875 \times 10^{-4}$.

B. validation

To validate the numerical method used in the present study, we first simulated the cases of a droplet sitting on the solid flat surface [see Fig. 3(a)]. A semicircular droplet is placed on a flat surface with an initial contact angle of 90°. The droplet will evolve to its equilibrium state at imposed contact angle. h_{max} is the height of the droplet above the flat surface. According to the conservation of mass, we get the analytical solution

$$\frac{h_{max}}{D_0} = \frac{1-\cos\theta}{2}\sqrt{\frac{\pi}{2\theta - \sin 2\theta}}. \tag{31}$$

Figure 3(b) shows good agreement between numerical and the analytical solutions for different contact angles.

To verify the numerical method, we considered the cases of a droplet resting on a membrane. First, a half droplet is place on a flat membrane. The membrane is mainly dominated by tension and bending can be neglected. In our simulations, the bending stiffness is very small, where $K_B = 1.0 \times 10^{-4}$. Because of the Laplace pressure, the droplet deforms the membrane and a bulge appears (see Fig. 4). According to the study of Schulman *et al.* [48], there are two angles to quantify the droplet and membrane geometries: θ_d and θ_b. Analogous to a Neumann construction, the forces at the triple point are balanced, i.e.,

$$\boldsymbol{\sigma} + \boldsymbol{T}_{out} + \boldsymbol{T}_{in} = \boldsymbol{0}, \tag{32}$$

where

$$|\boldsymbol{T}_{out}| = |\boldsymbol{T}_{in}| + |\boldsymbol{\sigma}|\cos\theta_{eq}. \tag{33}$$

It is a fact that the membrane is flat outside the droplet. A vertical force balance yields

$$\frac{|\boldsymbol{T}_{in}|}{|\boldsymbol{\sigma}|} = \frac{\sin\theta_d}{\sin\theta_b}. \tag{34}$$

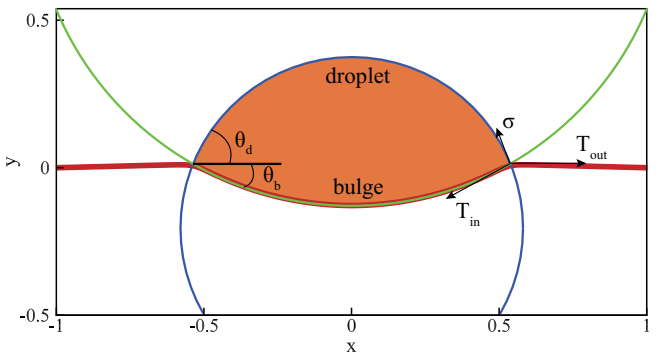

FIG. 4. A droplet with contact angle θ_{eq} rests on a membrane at $t = 100T_{ref}$. The red, blue, and green solid lines represent membrane profile, the fitted circle of the droplet profile, and the fitted circle of the bulge, respectively.

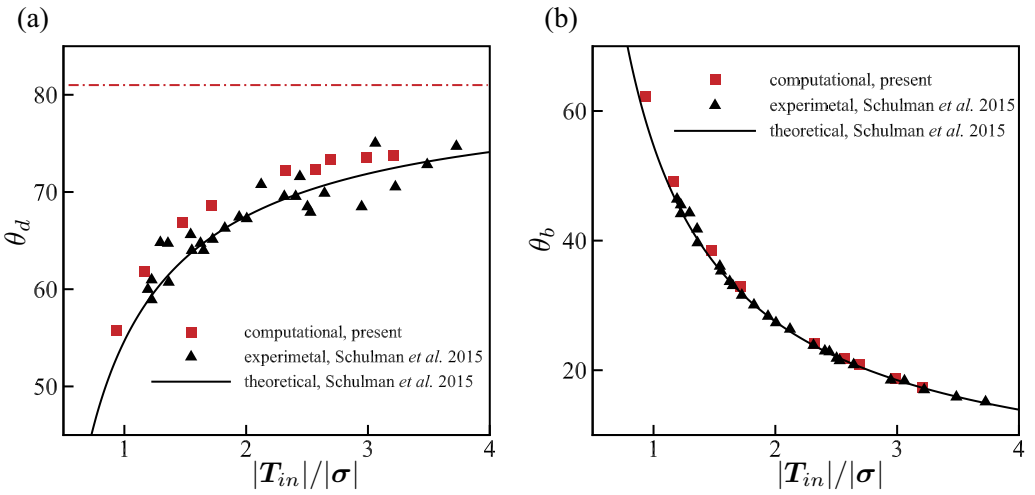

FIG. 5. (a) The droplet contact angle as a function of $|\boldsymbol{T}_{\text{in}}|/|\boldsymbol{\sigma}|$. The red dash-dotted line represents the equilibrium contact angle $\theta_{\text{eq}} = 81^\circ$. (b) The bulge contact angle as a function of $|\boldsymbol{T}_{\text{in}}|/|\boldsymbol{\sigma}|$.

Moreover, according to the cosine law, we have

$$\cos\theta_d = \frac{1 + (|\boldsymbol{T}_{\text{out}}|/|\boldsymbol{\sigma}|)^2 - (|\boldsymbol{T}_{\text{in}}|/|\boldsymbol{\sigma}|)^2}{2|\boldsymbol{T}_{\text{out}}|/|\boldsymbol{\sigma}|}, \tag{35}$$

$$\cos\theta_b = \frac{(|\boldsymbol{T}_{\text{in}}|/|\boldsymbol{\sigma}|)^2 + (|\boldsymbol{T}_{\text{out}}|/|\boldsymbol{\sigma}|)^2 - 1}{2|\boldsymbol{T}_{\text{in}}||\boldsymbol{T}_{\text{out}}|/|\boldsymbol{\sigma}|^2}. \tag{36}$$

Combined with Eqs. (33), (35), and (36), angles θ_d and θ_b can be measured as a function of T_{in}/σ, which can be easily obtained through Eq. (34). Figure 5 shows good agreement between our computational results and Schulman's results. Our numerical method can successfully solve the problems of droplets interacting with flexible substrates.

IV. RESULTS AND DISCUSSION

To better understand how flexibility affects the droplet impact dynamics, we investigated the droplet impact on the superhydrophobic flexible plate. The equilibrium contact angle is $\theta_{\text{eq}} = 170^\circ$. Here we present some typical results. All key governing parameters are listed in Table I.

The simulated results are shown in Fig. 6. It is seen that the droplet impacting on the flexible substrate experienced an early jump compared with that on a rigid substrate. Due to symmetry, only half of the flow field was plotted. When droplet impacts on a rigid substrate, the droplet deforms to be flat and the kinetic energy begins to convert to the surface energy. After reaching its maximum spreading diameter at the spreading time $t_{\text{spr}} = 0.47$, the droplet begins to retract, and takes off at the contact time $t_{\text{ct}} = 1.54$. While droplet impacts on a flexible substrate, the kinetic energy would convert to both the surface energy and the elastic energy of the flexible substrate. It is seen that the spreading time in the flexible case is $t_{\text{spr}} = 0.45$, which is close to that of the rigid case. Due to the existence of elastic energy of the plate, the surface energy of the droplet is reduced, and D_{max} is significantly smaller compared to the rigid case. Then, the droplet begins to retract. The surface energy and elastic energy simultaneously transfer to kinetic energy of the droplet, leading to a more significant upward speed and bouncing off at $t_{\text{ct}} = 1.2$. The contact time is reduced by 22% compared to that of the rigid case.

TABLE I. The parameters in the simulations.

Density ratio	ρ_r	1000
Dynamic viscosity ratio	μ_r	100
Weber number	We	[0.2,64]
Reynolds number	Re	1000
Bending stiffness	K_B	[0.02,10]
Stretching stiffness	K_S	100
Mass ratio	M	0.1
Plate length	L_r	5

A. Contact time

For further understanding of drop impact dynamics, we have simulated a series of cases of different flexibilities and Weber numbers. In these cases, the Weber number is changed by specifying different impact velocity. Figure 7(a) shows t_{ct} as a function of We. It is seen that t_{ct} on the rigid substrate increases with We for We > 2. For the flexible cases, it seems that only when We is higher than a critical value $\text{We}_c \approx 8$, is the contact time smaller than that in the rigid case. Hence, when We $> \text{We}_c$, the flexibility contributes to contact time reduction.

Figure 7(b) shows t_{ct} as a function of F_r for different We. It is seen that for the cases with We $= 2$, $t_{\text{ct}} \approx 2$ and 1 when $F_r < 0.3$ and $F_r > 1$, respectively. Therefore the flexibility increases t_{ct} when the substrate is very flexible at We $= 2$. The reason is that at a small We, the kinetic energy of the droplet is small and the droplet would easily adhere to the flexible substrate due to the capillary and viscous forces. For the cases with We $= 8$, the kinetic energy of the droplet becomes larger. The contact time reaches a valley at $F_r = 1$. It seems that a proper flexibility may reduce t_{ct}. For the cases with We $=$ 16, the kinetic energy of the droplet becomes large. When

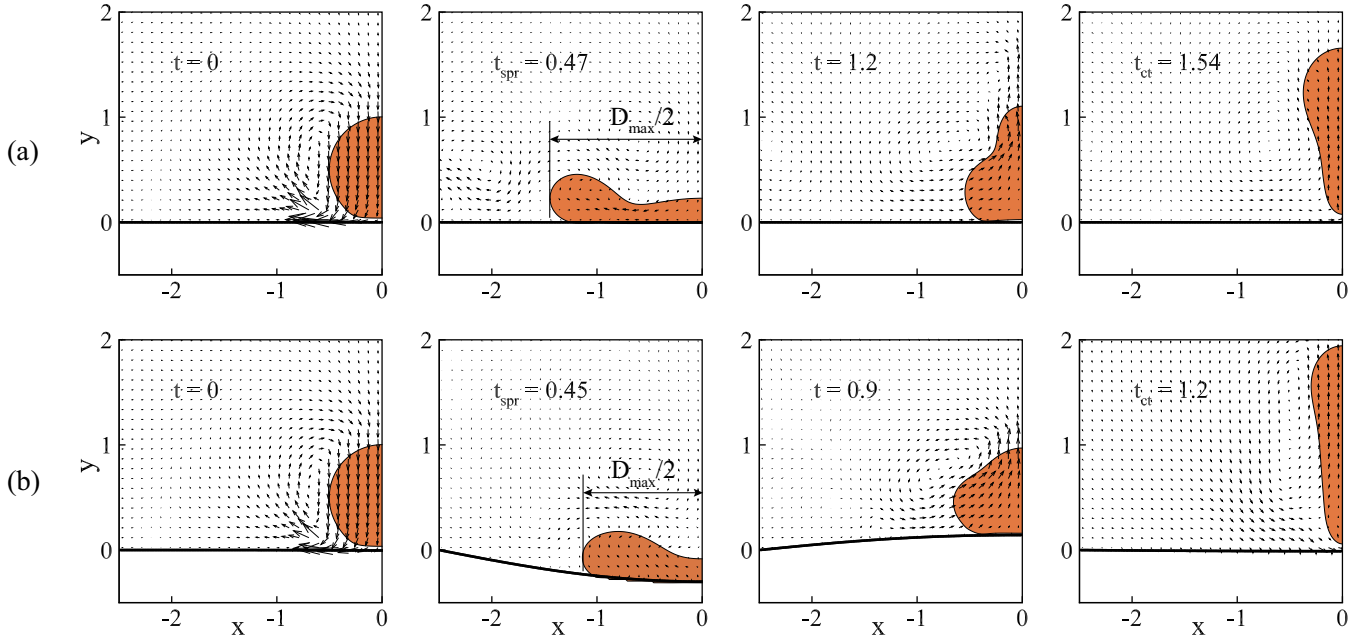

FIG. 6. Snapshots of the water droplet impact on (a) a rigid surface and (b) a flexible surface with $K_B = 1.0$ ($F_r = 0.99$). In both cases We $= 16$. The droplet profile is described by the contour line $\phi = 0.5$. $t_{\rm spr}$ is the spreading time at which the droplet reaches $D_{\rm max}$ and $t_{\rm ct}$ is the contact time at which the droplet leaves off the plate.

$F_r < 1$, the contact time $t_{\rm ct}$ becomes significantly smaller. For example, $t_{\rm ct} = 1.15$ at $F_r = 0.77$ (see the green circle) while $t_{\rm ct} = 1.53$ at $F_r = 10$ (see the black circle). Hence, under these circumstances, the flexibility does contribute to the reduction of $t_{\rm ct}$.

From Fig. 7(b) it is also seen that for $F_r \geqslant 2$, $t_{\rm ct}$ is approximately a constant for each We because when Fr $\geqslant 2$, the substrate is rigid and the elastic energy is almost negligible. In our simulations, only the cases with We < 20 are considered. At a larger We, maybe more kinetic energy of the droplet would convert into the elastic energy of the plate, which would accelerate the droplet in the upward direction. In this way, a pan-cake bouncing may appear. It is a such bouncing that the droplet leaves the plate only due to the elastic energy of the plate instead of the kinetic energy converted from the surface energy (see the experiments of Weisensee [19] for more detail). We will discuss this kind of bouncing in our future work.

For $F_r < 0.4$ and We $= 16$, the contact time is almost constant. Because K_S is fixed in our simulations, for the cases with small K_B, the stretching energy dominates the elastic energy of the substrate. The frequency ratio in Eq. (10) based on K_B seems not appropriate to quantify the elastic energy. In our following discussions, we would focus on the first-order natural frequency of the plate, in which K_B is dominant.

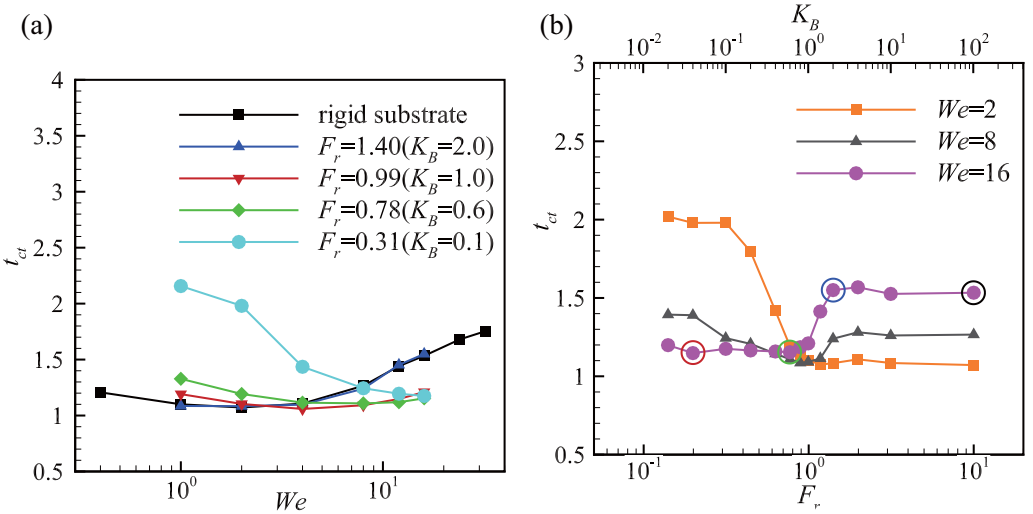

FIG. 7. (a) Contact time $t_{\rm ct}$ as a function of We for different K_B. (b) $t_{\rm ct}$ as a function of F_r for different We. Cases of $F_r = 10$ represent the cases with rigid substrate. Black, blue, green, and red circles represent the cases at $F_r = 10$, 1.4, 0.77, 0.2, respectively.

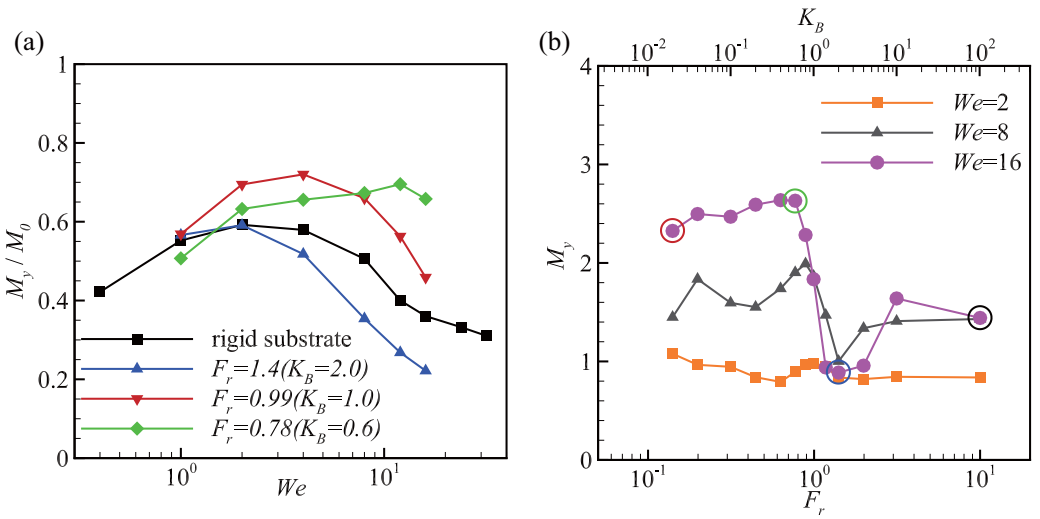

FIG. 8. (a) The coefficients of restitution $\frac{M_y}{M_0}$ as a function of We for different K_B. M_0 is the initial momentum of the droplet for each We. (b) Remaining upward momentum as a function of F_r for different We, and $F_r = 10$ represents the cases of droplets impacting on the rigid substrate.

B. Transfer of momentum

In this section, the transfer of momentum during the impact would be discussed. The remaining y-component momentum of the droplet M_y at the time of taking off as functions of We and Fr is shown in Fig. 8. For the rigid cases, a downward impact force is exerted on the substrate, and the droplet thus receives an upward reaction force. Moreover, due to the conversion of the surface energy to the kinetic energy of the droplet, the droplet will bounce off with the remaining upward momentum. M_y can be normalized by the reference momentum $M_{\text{drop}}U_{\text{ref}}$, where $M_{\text{drop}} = 0.25\pi D_0^2\rho_H$. It is noticed that the reference momentum is one of the physical quantities relevant to droplet properties but independent of impact velocities.

From Fig. 8(a), it is seen that for the rigid cases, the coefficient of restitution $\frac{M_y}{M_0}$ increases and then decreases as We increases. $\frac{M_y}{M_0}$ reaches its maximum value, 0.59, at We = 2. When We is small, e.g., We < 2, the kinetic energy of the droplet is small, and it becomes easier to adhere to the plate due to capillary and viscous forces. Thus, $\frac{M_y}{M_0}$ decreases as We decreases. When We is large, e.g., We > 2, $\frac{M_y}{M_0}$ decreases with We. This means that energy dissipation is also significant at larger We. For cases with $K_B = 2.0$, $\frac{M_y}{M_0}$ would decrease compared to that in the rigid case for We > 2. Furthermore, it is worth noting that when the flexibility is appropriate, e.g., $K_B \leqslant 1.0$, $\frac{M_y}{M_0}$ may increase substantially compared to its value in the rigid case.

From Fig. 8(b), it is seen that M_y is significantly influenced by F_r, especially at larger We. For the cases with We = 2, M_y increased slightly compared to that in the rigid case for different F_r. In addition, M_y reaches a peak at $F_r = 1$. It seems that a proper flexibility may increase the remaining momentum. For a large Weber number, e.g., We = 8, the peak is more obvious. However, a valley also appears at $F_r = 1.4$, where the momentum decreases. For cases with We = 16, as F_r increases, the momentum first increases a little bit, then dramatically decreases and later increases slightly. The reason for the dramatic decrease will be discussed below. It is also noted that for $F_r = 10$, M_y is the same as that in the case of We = 8. This means that at We = 16, the dissipation is large. It could be seen from Fig. 8(a) that $\frac{M_y}{M_0} = 0.36$ at We = 16, and $\frac{M_y}{M_0} = 0.51$ at We = 8. So when the Weber number is large enough, the plate with an appropriate flexibility would store more elastic energy, and reduce the energy dissipation.

The energy, momentum and deformation evolutions of the droplet are shown in Fig. 9 for the cases with We = 16. For the rigid case (see the black lines), Fig. 9(a) shows that the kinetic energy of the drop E_k decreases rapidly and then it reaches a valley with $E_k \approx 0$ at $t \approx 0.5$. In the moment E_k is almost completely converted into surface energy and viscosity dissipation. From Fig. 9(b) it also seen that $D_{\max}$ reaches a peak at the moment. After that, the droplet recoils and the surface energy is converted into the kinetic energy. Figure 9(c) shows that there is a plateau in the curve of the momentum at $t \in (0.4, 1)$. In the period, the horizontal momentum is important. When $t \in (1, 1.5)$, due to the symmetry, the horizontal momentum collides with each other, turns to the vertical momentum, and produces a strong jet. Finally at $t_{\text{ct}} \approx 1.5$ the droplet eventually bounces off from the surface.

For the case of $F_r = 1.4$ (the blue lines in Fig. 9), $t_{\text{ct}} \approx 1.5$, which is identical to the rigid case but M_y is significantly reduced by about 38% compared to that in the rigid case [see Figs. 7(b) and 8(b)]. The kinetic energy evolution of the droplet is similar to that in the rigid case [see Fig. 9(a)]. From Fig. 9(b), it is seen that $t_{\text{spr}} \approx 0.5$. It seems that the flexibility does not affect t_{spr} [19] but it may decrease $D_{\max}$ significantly. We can also see that before the droplet reaches its $D_{\max}$, i.e., $t < t_{\text{spr}}$, the plate begins to move upward ($t \approx 0.3$), which accelerate the droplet upward until M_y reaches a peak [see Fig. 9(c)]. Nevertheless, the upward momentum obtained by the droplet is not enough to make it bounce off directly. Moreover, from Fig. 9(c), it is seen that the increase

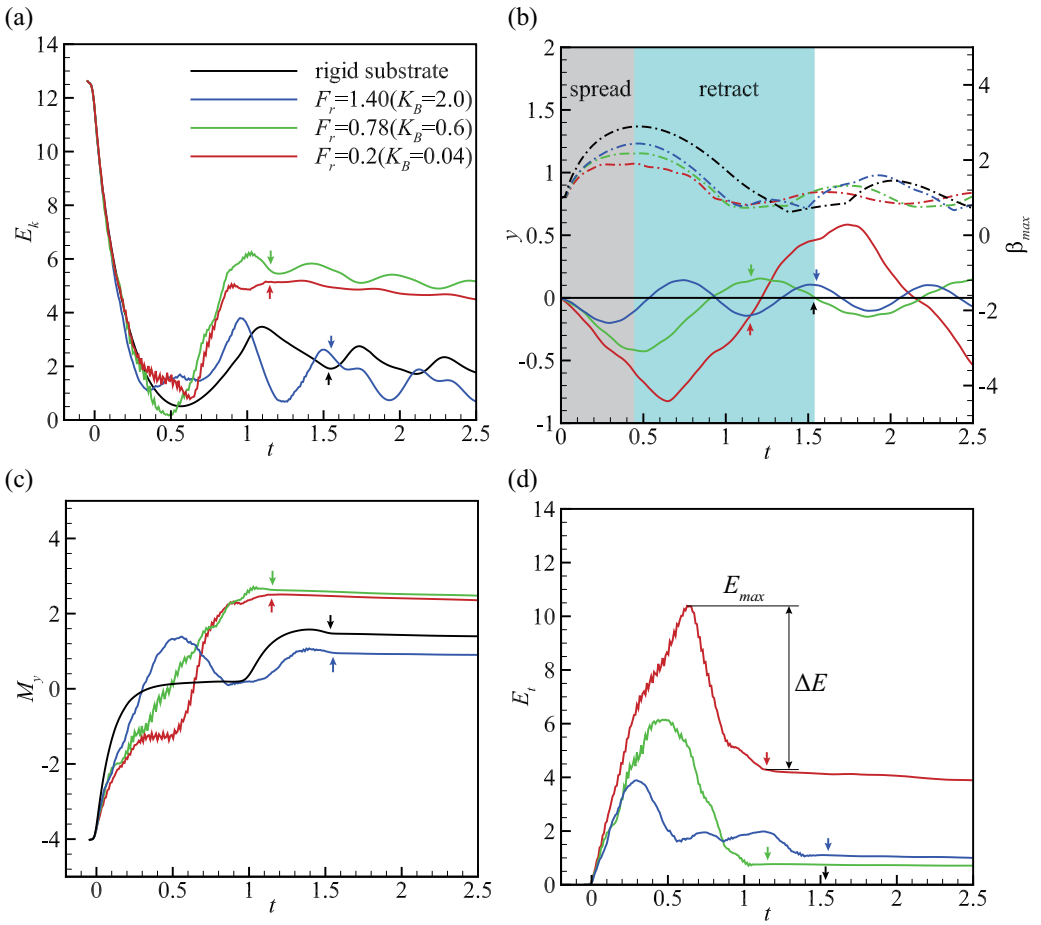

FIG. 9. (a) The evolution of the kinetic energy of the droplet for different F_r. (b) The evolution of total energy of the flexible substrate, including the kinetic energy, the bending energy, and the stretching energy. (c) The evolution of M_y. (d) The evolution of the displacement of the center of the plate in the y direction (solid lines) and the evolution of $D_{\max}$ (dash-dotted lines). The short vertical arrows on each line in (a, b, c, d) represents $t = t_{\rm ct}$. The shaded areas in (d) represent the "spread" and "retract" stages of a droplet when it impacts on a surface. In all cases We = 16.

of M_y, i.e., $\frac{dM_y}{dt}$ is slower than that in the rigid case because the flexible substrate also moves downward shortly after the impact. Similar phenomena also exist in the other flexible cases. The droplet converts its kinetic energy to the surface energy and elastic energy simultaneously, and the elastic energy of the plate is increasing shortly after the impact [see Fig. 9(d)]. The flexible substrate vibrates for approximately two cycles until the droplet completely bounces off. In this situation, less deformation energy of the flexible substrate is converted to the kinetic energy of the droplet. The bouncing is mainly due to the conversion of surface energy to the kinetic energy of the droplet. Moreover, multiple oscillations result in more dissipation, and finally when the droplet bounces off, M_y is reduced compared with that in the rigid case.

For the case of $F_r = 0.77$ (the green lines in Fig. 9), the contact time is reduced by about 25%, and the remaining upward momentum is increased by about 78% compared with that in the rigid case [see Figs. 7(b) and 8(b)]. From Fig. 9(b), we can see that when y reaches a valley at $t \approx 0.5$, the diameter of the droplet reaches $D_{\max}$. Then the droplet begins to retract, and the substrate moves upward simultaneously. This means that the surface to kinetic and elastic to kinetic energy conversions are synchronous. From Fig. 9(c), It is seen that M_y seems to increase at a constant speed, e.g., $\frac{dM_y}{dt} = \text{const}$, until the droplet detaches from the flexible plate. Figure 9(d) shows that most of the energy stored in the elastic substrate returns to the droplet again in one cycle of the vibration. The elastic energy conversion efficiency can be quantified by

$$\eta = \frac{\Delta E}{E_{\max}}, \tag{37}$$

where $E_{\max}$ is the maximal energy absorbed by the substrate, and ΔE is the energy that the plate returns to the droplet again. η as a function of F_r is shown in Fig. 10(a). In this case $\eta = 0.876$, which is high although $E_{\max}$ is not so high. It is noted that η reaches a valley at $F_r = 1.18$. The reason is similar to that of the valley of M_y [see Fig. 8(b)]. In this situation, the flexible substrate vibrates for multiple cycles until the droplet bounces off. Less elastic energy is converted to kinetic energy of the droplet. Moveover, the dissipation is large.

For the case of $F_r = 0.20$, t_{ct} and M_y are almost the same as those in the case of $F_r = 0.77$. It is seen from Fig. 10(b) that when K_B is small, $\frac{E_s}{E_b}$ is large. It seems that the stretching energy is dominant over the bending energy. As

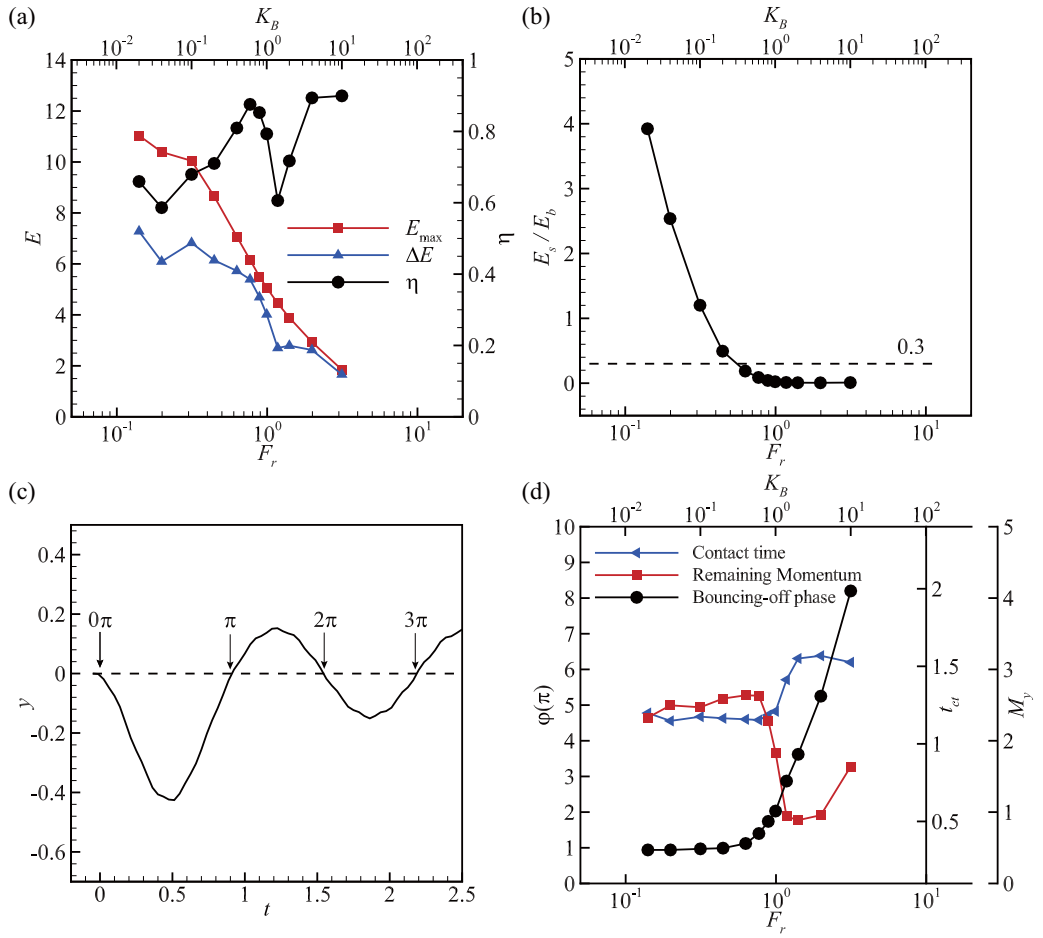

FIG. 10. (a) The elastic energy conversion efficiency η as a function of the F_r. (b) The ratio of the stretching energy to the bending energy $\frac{E_s}{E_b}$ as a function of F_r. (c) Definition of the phase according to the movement of the center of the substrate. (d) The bouncing-off phase ϕ, at which the droplet leaves the surface, t_{cr} and M_y as functions of F_r. In all cases We = 16.

mentioned above, for a small bending stiffness, Eq. (10) is not appropriate. The actual frequency ratio of the plate vibration now is mainly controlled by K_S, which is fixed to be 100 in all simulations. So for $F_r < 0.77$, the real frequency ratio is almost constant and corresponding t_{ct} and M_y are constant.

The evolution of the center of the substrate is shown in Fig. 10(c). The phase of the plate can be defined through the curve. Suppose the phases at $y = 0$ are $0, \pi, 2\pi$,..... chronologically. Then the phase when the droplet bounces off can be obtained through a linear interpolation. The bouncing-off phase as a function of F_r is shown in Fig. 10(d). It is seen that to achieve a smaller t_{ct} and a larger M_y, the bouncing-off phase should fall within the range of $(\pi, 2\pi)$. It is also found that $F_r \approx 1/t_{\rm ctr}$ when the bouncing-off is in the range of $(\pi, 2\pi)$, where $t_{\rm ctr}$ is the contact time of droplets impact on the rigid surface at the same We.

In summary, to reduce t_{ct} and increase M_y, first the Weber number must be large enough to overcome the viscosity and capillary force. In our simulations, the critical value of the Weber number is about 8. Second the frequency ratio should satisfy $F_r \approx 1/t_{\rm ctr}$. Under this circumstance, the bouncing takes place in the phase range of $(\pi, 2\pi)$. In this range, the kinetic-surface and kinetic-elastic energy conversions are synchronous.

C. Scaling laws for $\beta_{\rm max}$ and $\delta_{\rm max}$

To further study the role of flexibility on the dynamics of droplet impact, we investigated the effect of flexibility on the maximal spreading diameter, $\beta_{\rm max} = D_{\rm max}/D_0$, and maximal deflection of the center of the substrate $\delta_{\rm max} = \Delta_{\rm max}/D_0$. First of all, we numerically studied the maximum spreading diameter of a droplet impact on a rigid surface. In our 2D simulations, analogous to the study of Chandra *et al.* [11], according to energy conservation between the kinetic energy and the surface energy of the droplet, we have

$$\rho_H D_0^2 U^2 \sim \sigma D_{\rm max}, \tag{38}$$

according to the definitions of $\beta_{\rm max}$ and We, it yields

$$\beta_{\rm max} \sim {\rm We}. \tag{39}$$

Analogous to the study of Clanet *et al.* [12], according to volume conservation and equivalent gravitational acceleration, we have

$$D_0^2 \sim D_{\rm max} h, \quad h \sim \sqrt{\sigma/\rho_H g^*}, \quad g^* \sim U^2/D_0, \tag{40}$$

which is equivalent to

$$\beta_{\rm max} \sim {\rm We}^{1/2}. \tag{41}$$

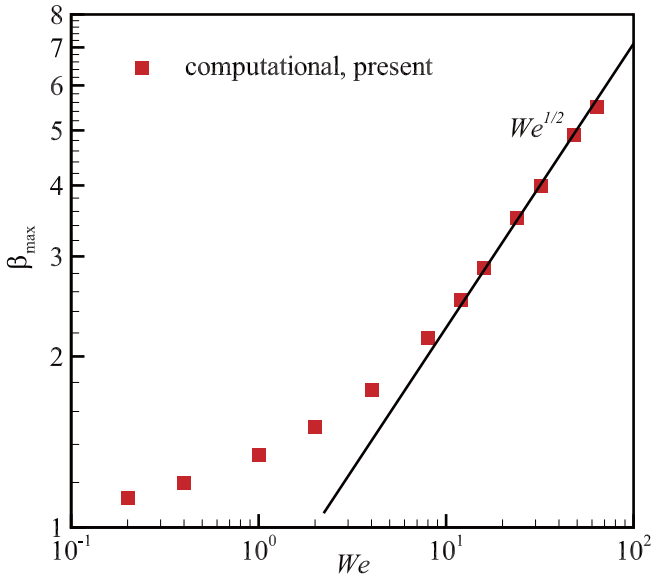

FIG. 11. The maximal spreading diameter ratio as a function of We. The solid black line represents the equivalent gravitational acceleration scaling rate $We^{1/2}$. In all cases, the surfaces are rigid.

It is seen from Fig. 11 that for We > 10, the scaling law of $We^{1/2}$ agrees well with the numerical results. More details about D_{max} of 3D droplets impact on rigid surfaces have been discussed in the literature [13,14]. Here, we focus on the role of flexibility in the spreading diameter of the droplet and deflection of the plate.

The maximal deflection of the center of the flexible substrate was investigated. Figure 12(a) shows that the maximal deflection decreases as K_B increases for all We. The deflection is relevant to the oscillations of the plate and droplet. The droplet-substrate interaction can be modeled as interaction between two spring oscillators. The flexible substrate could be modeled as a spring with stiffness k_s and an equivalent mass m_s which satisfy [18,19,49]

$$f_s = \frac{\omega_s}{2\pi} = \frac{1}{2\pi}\sqrt{\frac{k_s}{m_s}}, \tag{42}$$

where $k_s = 48EI/L^3$, corresponding to the simply supported boundary condition on both sides of the plate. According to Eq. (9), the equivalent mass $m_s = k_s/\omega_s^2 = 48/\pi^4\rho_s hL \simeq 0.5\rho_s hL$ for the first-order mode $n = 1$. Similarly, the droplet

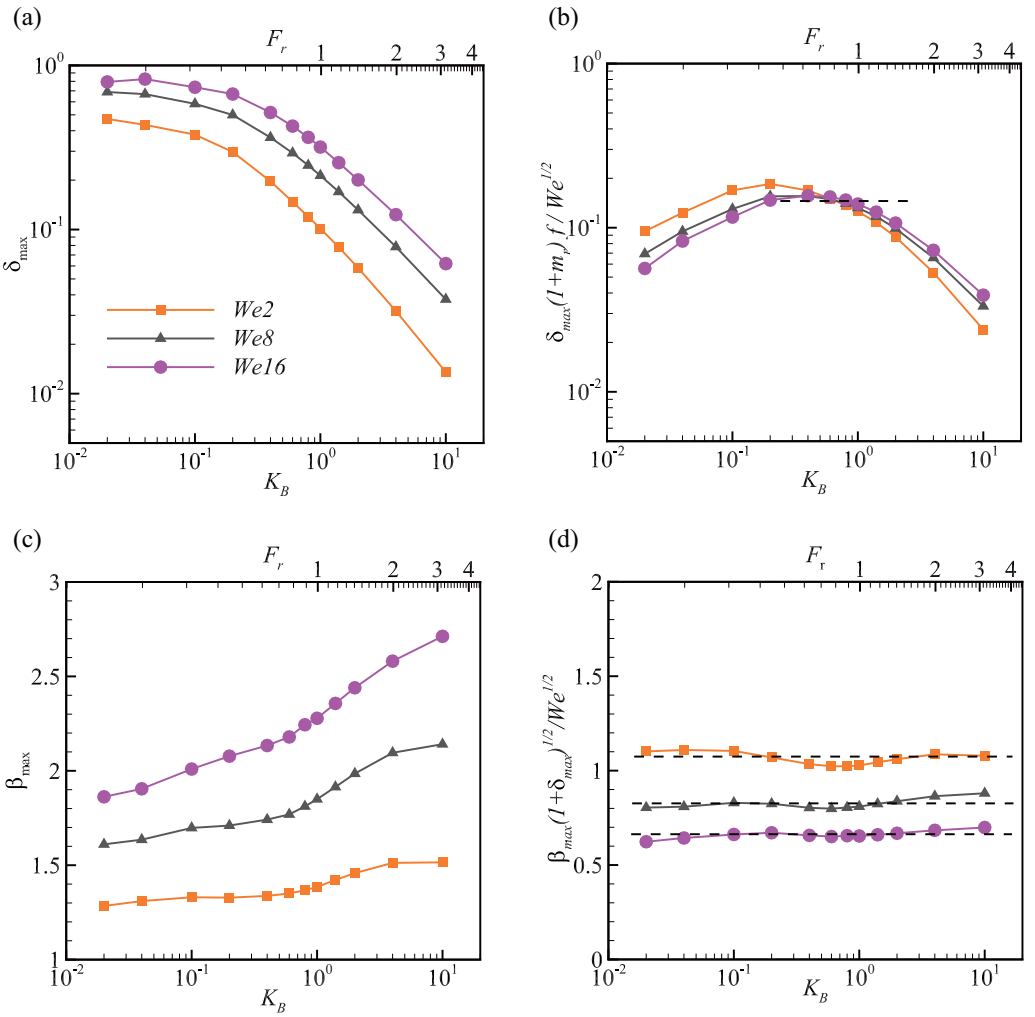

FIG. 12. (a) The maximal deflection of the center of the substrate as a function of K_B for different We. (b) Normalized deflection as a function of K_B. (c) β_{max} as a function of K_B for different We. (d) Normalized diameter ratio as a function of K_B.

can also be modeled as another spring [49]. We have

$$f_d = \frac{\omega_d}{2\pi} = \frac{1}{2\pi}\sqrt{\frac{k_d}{m_d}}, \tag{43}$$

where m_d is equal to the mass of the droplet, i.e., $0.25\pi D_0^2\rho_H$. According to the study of Takaki *et al.* [50], the natural vibration frequency of a circular column droplet is proportional to the reciprocal of its characteristic time $\sqrt{\rho_H D_0^3/\sigma}$, which is the reference frequency f_{ref} in our simulations. Here, we define $f_d = f_{\text{ref}}$. Then, we have $k_d = (2\pi f_d)^2 m_d$. The two-degree-of-freedom system can be described by

$$m_s\frac{d^2y_s}{dt^2} = -k_s x_s + k_d(y_d - y_s), \tag{44}$$

$$m_d\frac{d^2y_d}{dt^2} = -k_d(y_d - y_s), \tag{45}$$

where y_s and y_d are the displacements of the substrate and the droplet, respectively. This system has two natural frequencies:

$$\omega^2 = (2\pi f)^2 = \tfrac{1}{2}\big(\omega_d^2 + \omega_s^2 + k_d/m_s \pm \sqrt{\left(\omega_d^2 + \omega_s^2 + k_d/m_s\right)^2 - 4\omega_d^2\omega_s^2}\big). \tag{46}$$

The system would vibrate at the smaller frequency. If both ends of Eq. (46) are divided by ω_d^2, we have

$$\bar{f}^2 = \tfrac{1}{2}\big(1 + F_r^2 + 1/m_r\big)\big(1 - \sqrt{1-\epsilon}\big), \tag{47}$$

where $m_r = m_s/m_d$, $F_r = f_s/f_d$, and $\epsilon = 4F_r^2/(1 + F_r^2 + 1/m_r)^2$. For small K_B, the substrate velocity just after impact, U_s, scales as the one for a completely inelastic collision [18] $(m_d + m_s)U_s = m_d U$. So the maximal deflection of the plate can be yield as

$$\Delta_{\max} f \sim U_s, \tag{48}$$

according to the definition of U_s, it yields

$$\delta_{\max}(1 + m_r)\bar{f} \sim \text{We}^{1/2}. \tag{49}$$

Figure 12(b) shows the normalized deflection as a function of K_B. It is seen that at moderate K_B [$K_B \in (0.25, 1)$], the curves for different We almost collapse into a single horizontal line (the dashed line). At a large K_B, the deflection is smaller than the theoretical one in Eq. (48), which is represented by the dashed line. The reason is that under this circumstance, the assumption of completely inelastic collision is not appropriate. It is seen from Fig. 9(b) that for $K_B = 2.0$, when the substrate reaches its lowest point, the droplet is still moving downwards. It is inconsistent with the system moving together in one direction after a completely inelastic collision. That may lead to a discrepancy. At a small K_B, the actual frequency of the substrate is larger due to the fixed K_S, so the actual deflection is less than that obtained from Eq. (48).

Then we studied the maximal spreading diameter. Figure 12(c) shows that $\beta_{\max}$ increases as K_B increases for all simulated We. Similar to Eq. (40), taking into account the deflection of the substrate, we get

$$D_0^2 \sim D_{\max} h, \quad h \sim \sqrt{\sigma/\rho_H g^*}, \quad g^* \sim U^2/(D_0 + \Delta_{\max}), \tag{50}$$

which is equivalent to

$$\beta_{\max} \sim \text{We}^{1/2}/(1 + \delta_{\max})^{1/2}. \tag{51}$$

Figure 12(d) shows that curves agree well with different horizontal lines for different We. Hence, Eq. (51) is able to well predict the spreading diameter while taking into account the effects of flexibility and mass ratio. It is also noted that the data for different We do not collapse into one single horizontal line. The reason is that for $\text{We} < 10$, the deformation of the droplet is small, so the shape of the droplet is approximately an ellipsoid. The assumption of Eq. (40) no longer holds. Moreover, the scaling law for small We does not fit the law of $\text{We}^{1/2}$(see Fig. 11).

D. The effect of flexibility on droplet bouncing for different wettability

The cases investigated above all describe droplets impacting on superhydrophobic surfaces, where $\theta_{\text{eq}} = 170^\circ$. We found that if the substrate has appropriate flexibility, then the droplet could get more upward momentum and shorter contact time. We are also curious whether the flexibility would promote the bouncing of the droplets impact on the substrates with different wettability. Some cases with different wettability were simulated and the results are presented in Fig. 13. From Fig. 13(a) we can see that for superhydrophobic surfaces, the droplets will bounce off for all simulated We. For $\text{We} = 1$, and $\theta_{\text{eq}} \leqslant 130^\circ$, the kinetic energy is too small to overcome the capillary and viscous force, so it adheres to the surface. Similar phenomena has been found in cases of $\theta \leqslant 110^\circ$. However, Fig. 13(b) shows that the flexibility would help the droplets to bounce off. For $\text{We} > 4$, the droplets could bounce off at smaller contact angles due to the existence of flexibility. Here, we only discuss it qualitatively and more detailed discussions will be in our future work.

V. CONCLUSION

Droplets impact on the flexible substrate was investigated numerically. We developed a numerical method that can handle the fluid structure interaction with wetting boundary condition. Our results show that to reduce the contact time t_{ct} and increase the remaining upward momentum M_y, two conditions should be satisfied. First, We should be higher than We_c to overcome the viscosity and capillary forces. In our simulations, $\text{We}_c \approx 8$. Second, the frequency ratio should satisfy $F_r \approx 1/t_{\text{ctr}}$. Under this circumstance, the bouncing takes place in the phase range of $(\pi, 2\pi)$. In addition, the kinetic energy converts into the surface energy of the droplet and the elastic energy of the plate simultaneously, and vice versa. In this way, the droplet is able to obtain more kinetic energy and larger upward acceleration before it bounces off the plate compared to the case of the rigid plate.

The influences of flexibility on the $\delta_{\max}$ and $\beta_{\max}$ were investigated. $\delta_{\max}$ and $\beta_{\max}$ are relevant to the oscillations of the plate and droplet. The droplet-substrate interaction was modeled as the interaction between two spring oscillators. Through the model, a scaling law of $\delta_{\max}$ was proposed. It is found that at moderate K_B, the numerical results for different

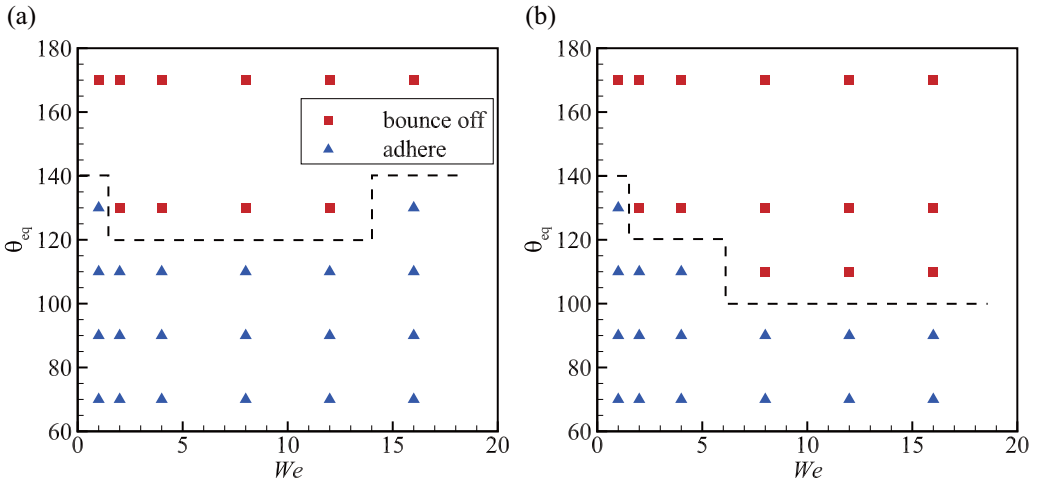

FIG. 13. "bounce off" and "adhere" phase diagram for different We and wettability, characterized by the contact angle θ. (a) Droplets impact on a rigid surface. (b) Droplets impact on a flexible surface. In all cases of (b) $K_B = 0.6$ ($F_r = 0.77$).

We agree well with the results obtained from that scaling law. Moreover, a scaling law of $\beta_{\max}$ was also proposed.

Finally, the effect of flexibility on the droplet bouncing for different wettability was qualitatively investigated. It is found that the flexibility could effectively help the droplets bounce off at the smaller contact angles.

In our study, the simulations were limited to 2D cases to save computational resources. However, our 2D model study is reasonable, and it may incorporate enough physics to contribute to a better understanding of the interaction between droplets and deformable moving boundaries.

ACKNOWLEDGMENTS

This work was supported by the Natural Science Foundation of China (NSFC) under Grants No. 11872064 and No. 11621202. H.H. is supported by NSFC Grant No. 11772326.

APPENDIX: CONTACT ANGLE MODEL

Suppose $\boldsymbol{x}_s$ is one of the outside points which are most close to the beam (suppose the droplet is inside). $\boldsymbol{x}_{\rm BI}$ is the projection of $\boldsymbol{x}_s$ on the beam (the red line) (see Fig. 14). At each time step, we have to update ϕ at $\boldsymbol{x}_s$ to ensure that ϕ_w, i.e., $\phi(\boldsymbol{x}_{\rm BI})$ satisfies Eq. (3).

Here, the weighted least square method is adopted to enforce Eq. (3) [43]. In the method, ϕ in the vicinity of $\boldsymbol{x}_{\rm BI}$ can be approximated by Nth-degree polynomial Φ as follows:

$$\phi(\xi,\eta) \approx \Phi(\xi,\eta) = \sum_{i=0}^{N}\sum_{j=0}^{N} c_{ij}\xi^i\eta^j, \quad i+j \leqslant N, \tag{A1}$$

where $\xi = x - x_{\rm BI}$, $\eta = y - y_{\rm BI}$, and c_{ij} is unknown coefficients. To determine the values of c_{ij}, ϕ on the blue-circle points (see Fig. 14) have to be used. Then the weighted square error is defined as

$$\epsilon = \sum_{m=1}^{M} w_m^2[\Phi(\xi_m,\eta_m) - \phi_m]^2, \tag{A2}$$

where M is the number of the blue-circle points in Fig. 14), ϕ_m is the mth point and w_m is the weight function. Here, for $m = 1$, ϕ_1 denotes $\phi(\boldsymbol{x}_s)$, which has to be determined. Besides, a cosine weight function is adopted, i.e., $w_m = \frac{1}{2}[1 + \cos(\frac{\pi d_m}{R})]$, where d_m is the distance between the mth data point and $\boldsymbol{x}_{\rm BI}$. A linear relationship between c_{ij} and ϕ_m can be determined by minimizing the weighted square error, i.e., we have $\boldsymbol{c} = \boldsymbol{A}\boldsymbol{\phi}$. According to Taylor's expansion, c_{ij} is also related to the local derivatives of $\boldsymbol{x}_{\rm BI}$ and we have

$$c_{00} = \phi|_{\rm BI}, \quad c_{10} = \left.\frac{\partial\phi}{\partial x}\right|_{\rm BI}, \quad c_{01} = \left.\frac{\partial\phi}{\partial y}\right|_{\rm BI}. \tag{A3}$$

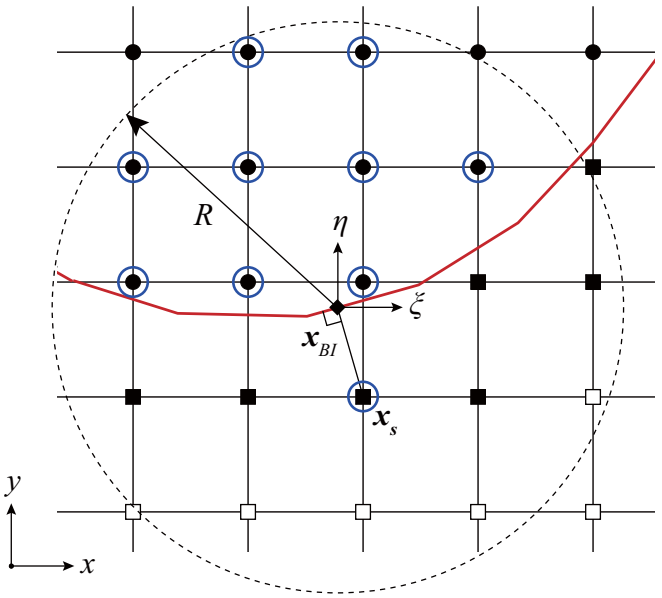

FIG. 14. Schematic of the least square method. $\boldsymbol{x}_{\rm BI}$ is the projection of $\boldsymbol{x}_s$ on the beam (the red line). A local coordinates (ξ,η) is established with origin at $\boldsymbol{x}_{\rm BI}$. The large dotted circle denote a range of $|\boldsymbol{x} - \boldsymbol{x}_{\rm BI}| < R$, where R is a specified radius. Blue circle points are inside the range. Discs (•) denotes the fluid nodes inside the beam (suppose the droplet is inside).

Hence,

$$\frac{\partial \phi}{\partial n} = n_x \frac{\partial \phi}{\partial x}\bigg|_{\mathrm{BI}} + n_y \frac{\partial \phi}{\partial y}\bigg|_{\mathrm{BI}} = n_x c_{10}(\phi_m) + n_y c_{01}(\phi_m). \quad \text{(A4)}$$

Combining with the boundary condition, i.e., Eq. (3), the unknown ϕ_1, i.e., $\phi(\boldsymbol{x}_s)$, together with ϕ_w, could be obtained. In this way, Eq. (3) is enforced.

[1] T. Gilet and L. Bourouiba, Fluid fragmentation shapes rain-induced foliar disease transmission, J. R. Soc. Interface **12**, 20141092 (2015).

[2] L. Mishchenko, B. Hatton, V. Bahadur, J. A. Taylor, T. Krupenkin, and J. Aizenberg, Design of ice-free nanostructured surfaces based on repulsion of impacting water droplets, ACS Nano **4**, 7699 (2010).

[3] A. Fraters, M. van den Berg, Y. de Loore, H. Reinten, H. Wijshoff, D. Lohse, M. Versluis, and T. Segers, Inkjet Nozzle Failure by Heterogeneous Nucleation: Bubble Entrainment, Cavitation, and Diffusive Growth, Phys. Rev. Appl. **12**, 064019 (2019).

[4] D. Caviezel, C. Narayanan, and D. Lakehal, Adherence and bouncing of liquid droplets impacting on dry surfaces, Microfluid. Nanofluid. **5**, 469 (2008).

[5] M. H. K. Schaarsberg, I. R. Peters, M. Stern, K. Dodge, W. W. Zhang, and H. M. Jaeger, From splashing to bouncing: The influence of viscosity on the impact of suspension droplets on a solid surface, Phys. Rev. E **93**, 062609 (2016).

[6] D. Richard, C. Clanet, and D. Quéré, Surface phenomena: Contact time of a bouncing drop, Nature **417**, 811 (2002).

[7] J. C. Bird, R. Dhiman, H.-M. Kwon, and K. K. Varanasi, Reducing the contact time of a bouncing drop, Nature **503**, 385 (2013).

[8] A. Gauthier, S. Symon, C. Clanet, and D. Quéré, Water impacting on superhydrophobic macrotextures, Nat. Commun. **6**, 8001 (2015).

[9] Y. Liu, M. Andrew, J. Li, J. M. Yeomans, and Z. Wang, Symmetry breaking in drop bouncing on curved surfaces, Nat. Commun. **6**, 10034 (2015).

[10] Y. Liu, L. Moevius, X. Xu, T. Qian, J. M. Yeomans, and Z. Wang, Pancake bouncing on superhydrophobic surfaces, Nat. Phys. **10**, 515 (2014).

[11] S. Chandra and C. T. Avedisian, On the collision of a droplet with a solid surface, Proc. R. Soc. London A **432**, 13 (1884).

[12] C. Clanet, C. Béguin, D. Richard, and D. Quéré, Maximal deformation of an impacting drop, J. Fluid Mech. **517**, 199 (2004).

[13] N. Laan, K. G. de Bruin, D. Bartolo, C. Josserand, and D. Bonn, Maximum Diameter of Impacting Liquid Droplets, Phys. Rev. Appl. **2**, 044018 (2014).

[14] J. Lee, N. Laan, K. G. de Bruin, G. Skantzaris, N. Shahidzadeh, D. Derome, J. Carmeliet, and D. Bonn, Universal rescaling of drop impact on smooth and rough surfaces, J. Fluid Mech. **786**, R4 (2016).

[15] S. Mangili, C. Antonini, M. Marengo, and A. Amirfazli, Understanding the drop impact phenomenon on soft PDMS substrates, Soft Matter **8**, 10045 (2012).

[16] L. Chen, E. Bonaccurso, P. Deng, and H. Zhang, Droplet impact on soft viscoelastic surfaces, Phys. Rev. E **94**, 063117 (2016).

[17] C. J. Howland, A. Antkowiak, J. R. Castrejón-Pita, S. D. Howison, J. M. Oliver, R. W. Style, and A. A. Castrejón-Pita, It's Harder to Splash on Soft Solids, Phys. Rev. Lett. **117**, 184502 (2016).

[18] T. Vasileiou, J. Gerber, J. Prautzsch, T. M. Schutzius, and D. Poulikakos, Superhydrophobicity enhancement through substrate flexibility, Proc. Natl. Acad. Sci. USA **113**, 13307 (2016).

[19] P. B. Weisensee, J. Tian, N. Miljkovic, and W. P. King, Water droplet impact on elastic superhydrophobic surfaces, Sci. Rep. **6**, 30328 (2016).

[20] L. Huang, J. Song, X. Wang, C. Zhao, Z. Liu, and J. Liu, Soft elastic superhydrophobic cotton: A new material for contact time reduction in droplet bouncing, Surf. Coat. Technol. **347**, 420 (2018).

[21] M. Pegg, R. Purvis, and A. Korobkin, Droplet impact onto an elastic plate: A new mechanism for splashing, J. Fluid Mech. **839**, 561 (2018).

[22] A. De Rosis, A lattice Boltzmann model for multiphase flows interacting with deformable bodies, Adv. Water Resour. **73**, 55 (2014).

[23] A. Fakhari and D. Bolster, Diffuse interface modeling of three-phase contact line dynamics on curved boundaries: A lattice Boltzmann model for large density and viscosity ratios, J. Comput. Phys. **334**, 620 (2017).

[24] A. Fakhari, T. Mitchell, C. Leonardi, and D. Bolster, Improved locality of the phase-field lattice-Boltzmann model for immiscible fluids at high density ratios, Phys. Rev. E **96**, 053301 (2017).

[25] H. Liang, J. Xu, J. Chen, H. Wang, Z. Chai, and B. Shi, Phase-field-based lattice Boltzmann modeling of large-density-ratio two-phase flows, Phys. Rev. E **97**, 033309 (2018).

[26] Y. Hu, D. Li, and X. Niu, Phase-field-based lattice Boltzmann model for multiphase ferrofluid flows, Phys. Rev. E **98**, 033301 (2018).

[27] K. Connington and T. Lee, Lattice Boltzmann simulations of forced wetting transitions of drops on superhydrophobic surfaces, J. Comput. Phys. **250**, 601 (2013).

[28] D. Jacqmin, Calculation of two-phase Navier–Stokes flows using phase-field modeling, J. Comput. Phys. **155**, 96 (1999).

[29] B. S. Connell and D. K. Yue, Flapping dynamics of a flag in a uniform stream, J. Fluid Mech. **581**, 33 (2007).

[30] F.-B. Tian, H. Luo, L. Zhu, and X.-Y. Lu, Interaction between a flexible filament and a downstream rigid body, Phys. Rev. E **82**, 026301 (2010).

[31] L. Wang and F.-b. Tian, Numerical simulation of flow over a parallel cantilevered flag in the vicinity of a rigid wall, Phys. Rev. E **99**, 053111 (2019).

[32] M. Geier, A. Fakhari, and T. Lee, Conservative phase-field lattice Boltzmann model for interface tracking equation, Phys. Rev. E **91**, 063309 (2015).

[33] J. F. Doyle, *Nonlinear Analysis of Thin-walled Structures: Statics, Dynamics, and Stability* (Springer Science & Business Media, Berlin, 2013).

[34] K. W. Connington, T. Lee, and J. F. Morris, Interaction of fluid interfaces with immersed solid particles using the lattice

Boltzmann method for liquid–gas–particle systems, J. Comput. Phys. **283**, 453 (2015).
[35] G. A. Buxton, R. Verberg, D. Jasnow, and A. C. Balazs, Newtonian fluid meets an elastic solid: coupling lattice Boltzmann and lattice-spring models, Phys. Rev. E **71**, 056707 (2005).
[36] G. A. Buxton and N. Clarke, Computational phlebology: The simulation of a vein valve, J. Biol. Phys. **32**, 507 (2006).
[37] C. Tang, L. Zhu, G. Akingba, and X.-Y. Lu, Viscous flow past a collapsible channel as a model for self-excited oscillation of blood vessels, J. Biomech. **48**, 1922 (2015).
[38] R. Mei, L.-S. Luo, and W. Shyy, An accurate curved boundary treatment in the lattice Boltzmann method, J. Comput. Phys. **155**, 307 (1999).
[39] B. Yang and S. Chen, Simulation of interaction between a freely moving solid particle and a freely moving liquid droplet by lattice Boltzmann method, Int. J. Heat Mass Transf. **127**, 474 (2018).
[40] A. S. Joshi and Y. Sun, Multiphase lattice Boltzmann method for particle suspensions, Phys. Rev. E **79**, 066703 (2009).
[41] B. Wen, C. Zhang, Y. Tu, C. Wang, and H. Fang, Galilean invariant fluid–solid interfacial dynamics in lattice Boltzmann simulations, J. Comput. Phys. **266**, 161 (2014).
[42] J.-H. Pan, M.-J. Ni, and N.-M. Zhang, A consistent and conservative immersed boundary method for MHD flows and moving boundary problems, J. Comput. Phys. **373**, 425 (2018).
[43] J. H. Seo and R. Mittal, A high-order immersed boundary method for acoustic wave scattering and low-Mach number flow-induced sound in complex geometries, J. Comput. Phys. **230**, 1000 (2011).
[44] H. Luo, R. Mittal, X. Zheng, S. A. Bielamowicz, R. J. Walsh, and J. K. Hahn, An immersed-boundary method for flow–structure interaction in biological systems with application to phonation, J. Comput. Phys. **227**, 9303 (2008).
[45] P. Lallemand and L.-S. Luo, Lattice Boltzmann method for moving boundaries, J. Comput. Phys. **184**, 406 (2003).
[46] L. Chen, Y. Yu, J. Lu, and G. Hou, A comparative study of lattice Boltzmann methods using bounce-back schemes and immersed boundary ones for flow acoustic problems, Int. J. Numer. Methods Fluids **74**, 439 (2014).
[47] D. E. Keyes, L. C. McInnes, C. Woodward, W. Gropp, E. Myra, M. Pernice, J. Bell, J. Brown, A. Clo, J. Connors *et al.*, Multiphysics simulations: Challenges and opportunities, Int. J. High Perform. Comput. Appl. **27**, 4 (2013).
[48] R. D. Schulman and K. Dalnoki-Veress, Liquid Droplets on a Highly Deformable Membrane, Phys. Rev. Lett. **115**, 206101 (2015).
[49] P. Chantelot, M. Coux, C. Clanet, and D. Quéré, Drop trampoline, Europhys. Lett. **124**, 24003 (2018).
[50] R. Takaki and K. Adachi, Vibration of a flattened drop. II. Normal mode analysis, J. Phys. Soc. Jpn. **54**, 2462 (1985).